Advanced Sensor and Energy Materials
Article In Press
Acceptation date : March 2025
https://doi.org/10.1016/j.asems.2025.100149
https://archimer.ifremer.fr/doc/00944/105566/

Archimer
https://archimer.ifremer.fr

Mid-infrared integrated spectroscopic sensor based on chalcogenide glasses: optical characterization and sensing applications

Meziani S. [1], Hammouti A. [1], Bodiou L. [1], Lorrain N. [1], Chahal R. [2], Bénardais A. [2], Courson Remi [3], Troles J. [2], Boussard-Pledel C. [2], Nazabal V. [2], Charrier J. [1, *]

[1] Univ Rennes, CNRS, Institut Foton-UMR 6082, 22305 Lannion, France
[2] CNRS UMR 6226 ISCR, Université de Rennes 1, 22302 Rennes, France
[3] Ifremer, Laboratoire Détection Capteurs et Mesures, F-29280 Plouzané, France

* Corresponding author : J. Charrier, email address : joel.charrier@univ-rennes.fr

Abstract :

A mid-infrared (mid-IR) spectroscopic sensor is developed using a chalcogenide glasses (ChGs) platform with a broad transmission band. The ridge ChGs waveguides were patterned via standard i-line photolithography and reactive ion etching, following the deposition of guiding and confinement layers through RF magnetron sputtering. The waveguides exhibit a wide transparency range from λ = 3.94 to 8.95 µm, with minimum propagation losses value of 2.5 dB/cm at λ = 7.58 µm. To validate the feasibility of the suggested sensor, a spectroscopic gas sensing experiment was performed using CO2, resulting in an estimated limit of detection (LoD) of 1.16%v at λ = 4.28 µm, achieved with an external confinement factor Γ of 6.5%. Additionally, liquid sensing experiment was carried out using isopropanol, obtaining a LoD of 300 ppmv at λ = 7.25 µm.

Please note that this is an author-produced PDF of an article accepted for publication following peer review. The definitive publisher-authenticated version is available on the publisher Web site.

1. Introduction

The mid-Infrared (mid-IR) wavelength range contains absorption bands of various toxic and polluting molecules, making the integration of mid-IR spectroscopy photonic circuits an attractive approach for the development of compact, low cost and smart sensors. However, the fabrication of these circuits requires the use of mid-IR transparent materials. Chalcogenide glasses (ChGs) show great potential for the design of such circuits. They display extended transparency that ranges from near-infrared to 20 µm, depending on their composition [1]. ChGs are covalently bonded materials that contain one or more chalcogen elements (sulfur, selenium, and tellurium), combined with elements from groups IV, V, and VI of the periodic table. By adjusting their elemental composition, different ChGs can be obtained with an extended transparency into the mid-IR, up to 11 µm for sulfides, 15 µm for selenides, and 20 µm for tellurides [2]. This wide transparency has particularly attracted the interest of the fiber optics industry for applications in the mid-IR [3,4]. Remarkable progress has been made to reach commercialization.

In addition to a wide transparency range in the mid-IR, ChGs possess other interesting properties regarding optical applications. Their refractive indexes, tunable over a wide range by changing their composition, are used in the shaping of various guiding structures, notably for the fabrication of multilayers entirely made of chalcogenide glasses [5–7]. This characteristic allows the fabrication of gradient index structures, which are particularly useful in the design of lenses for thermal imaging [8]. Furthermore, they can also be doped with rare earth ions, some of which can emit in the mid-IR, such as praseodymium [9] and dysprosium [10]. This makes them interesting as a light source in the mid-IR, in addition to their non-linear refractive index, which is approximately two orders of magnitude higher than that of silica, associated with their low two-photon absorption in the NIR [11,12]. ChGs are also a suitable material for broadband mid-IR supercontinuum applications. ChGs have distinguished themselves with their thermal stability, owing to their low thermal coefficients of refractive index $\frac{dn}{dT}$ and their ease of shaping through precision molding. Chalcogenide phase change materials (PCMs), which transition from amorphous to crystalline states, are utilized in non-volatile memories and are increasingl applied in photonics. This includes uses in optical switching, photonic memory, and neuromorphic computing.

In terms of photonic integrated circuit (PIC), the interest in designing waveguide structures in chalcogenide glasses has already been demonstrated by several works. A rib waveguide in chalcogenide glasses ($Ge_{11.5}As_{24}Se_{64.5}$) deposited on magnesium fluoride showed propagation losses of less than 2 dB/cm at λ = 3.2 to 9.5 μm [13]. Similar losses values were reported for a waveguide in $Ge_{28}Sb_{12}Se_{60}$ deposited on silica with silver islands to enhance the sensing application at λ = 3.29 μm [14]. Other losses values of 0.6 dB/cm were reported between λ = 2.5 and 3.7 μm for a waveguide in zinc selenide (ZnSe) [15]. Using a guiding layer in $Ge_{11.5}As_{24}Se_{64.5}$ and a confinement layer in $Ge_{11.5}As_{24}S_{64.5}$, a microring resonator with a Q factor of 1.45×10^5 at mid-IR wavelength of 5.2 μm was reported [16]. The losses values reported at λ = 5.2 μm are 0.84 dB/cm in the microring resonator and 0.6 dB/cm in the straight waveguide. A well-recognized approach for PIC sensing is the evanescent wave absorption spectroscopy. It is based on the fraction of the field extending outside the waveguide core interacting with the targeted analyte [17]. It has been shown that the most appropriate parameter for calculating the fraction of the electric field interacting with the targeted analyte is the external confinement factor [18].

Several sensing experiments have also been reported using a ChGs platform. In 2018, Mittal et al. [19] deposited a 20 μm wide rib waveguide based on a chalcogenide layer (ZnSe) on a silica layer in order to detect isopropanol. To control the length of interaction between the analyte solution and the waveguide, filter paper was placed in contact with the waveguide. Among the measured concentrations, the one with

20% isopropanol in water is the smallest concentration reported. In 2019, Su et al. [20] reported a $Ge_{23}Sb_7S_{70}$ on SiO_2 waveguide, used for CH_4 sensing at λ = 3.31 µm. An evanescent field factor of 12.5% was found through numerical simulations. A polydimethylsiloxane (PDMS) cell was used to control the light-matter interaction over a length of 5 mm. The propagation losses values reported were 8 dB/cm. The limit of detection for methane was 10000 ppmv. In 2020, Qiao et al. [21] reported the detection of SF_6 gas at a low concentration of 10 ppmv using ChGs platform at λ = 10.55 µm.

In this paper, we focus on the transduction part of the integrated optical sensor. Both gas and liquid sensing, respectively CO_2 at λ = 4.28 µm and isopropanol at λ = 7.25 µm, are demonstrated using ChGs waveguides. The propagation losses assessment of the fabricated ridge waveguide is also carried out within the 4 to 4.6 and 6.9 to 8.95 µm wavelength ranges.

Prior to the fabrication step, the ridge waveguide structures were designed using a commercial software (*FIMMWAVE, Photon Design*) to obtain the geometrical dimensions, width (*w*) and height (*h*), ensuring single-mode propagation while optimizing the external confinement factor for evanescent field detection.

2. Experimental conditions

2.1 Materials and methods

A confinement layer of $Ge_{28.1}Sb_{6.3}Se_{65.6}$ with a thickness of 5 µm was grown on an n-type Si substrate using RF magnetron sputtering. A guiding layer of composition $Ge_{12.5}Sb_{25}Se_{62.5}$ was then deposited on top of the confinement layer. The refractive index values for the guiding and confinement layers remain relatively constant across the working wavelength range of λ = 3.94 to 8.95 µm and refractive indices of 2.77 and 2.49 were, respectively, measured using ellipsometry for these two layers.

Following thin film deposition, single mode ridge waveguides were fabricated using a conventional i-line photolithographic process. This was followed by a low-pressure dry etching procedure that combined reactive ion etching (RIE) and inductively coupled plasma (ICP) etching. The etching process used a gas mixture of 5 sccm CHF_3 at a pressure of 5 mTorr, with an ICP power of 75 W and an RF power of 25 W.

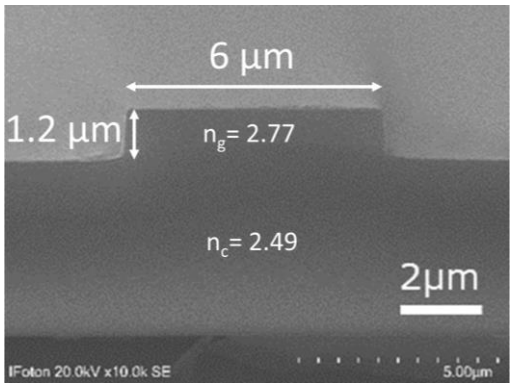

Fig. 1. SEM image of fabricated ChGs ridge waveguide with 6 µm width and 1.2 µm thickness from sample A.

It should be noted that to obtain single mode structure, waveguides dimensions were specifically designed for the targeted operating wavelengths. At λ = 4.28 µm, used for CO_2 sensing, the thickness of the guiding layer was $h_{4.28}$ = 1.2 µm, and the width of the waveguide was $w_{4.28}$ = 6 µm this sample is noted "sample A" (Fig. 1). In contrast, for sensing measurements at a wavelength of 7.25 µm, used for isopropanol sensing, the thickness of the guiding layer was increased to $h_{7.25}$ = 1.9 µm, and the width of the waveguide was $w_{7.25}$ = 8 µm. This sample is referred to as "Sample B". Table 1 summarizes the physical parameters of the fabricated samples.

Name	Sample A	Sample B
Wavelength range of operation (µm)	3.94–4.6	6.9–8.95
Core thikness (µm)	1.2	1.9
Core width (µm)	5	8
Γ_{TE}	9.1% (at λ= 4.28 µm)	5% (at λ= 7.25 µm)
Γ_{TM}	1.4% (at λ= 4.28 µm)	1.4% (at λ= 7.25 µm)
Sensing experiment	CO_2	Isopropanol

Table 1. Dimensions of waveguides used for operating wavelength ranges.

2.2 Optical bench and characterization of the guiding structures

A suitable mid-IR optical bench setup (Fig. 2) was assembled for the optical characterizations of the guiding structures. A tunable QCL source (*MIRCAT* from *Daylight Solutions*) was used with 1 cm^{-1} resolution and operating wavelength ranges from λ = 3.94 to 4.6 µm and λ = 6.9 to 11 µm. The input signal was coupled into the ridge waveguides using a chalcogenide glass fiber (Fig. 3a). The output signal from the waveguide was collimated into a detector using a mid-IR objective lens. To improve the signal-to-noise ratio, a lock-in technique was employed using chopping frequency of 70 Hz. The photolithography

mask used consists of several sets of waveguides of different lengths. This configuration allows propagation losses measurements using a non-destructive cut-back method as showed in the Fig. 3b.

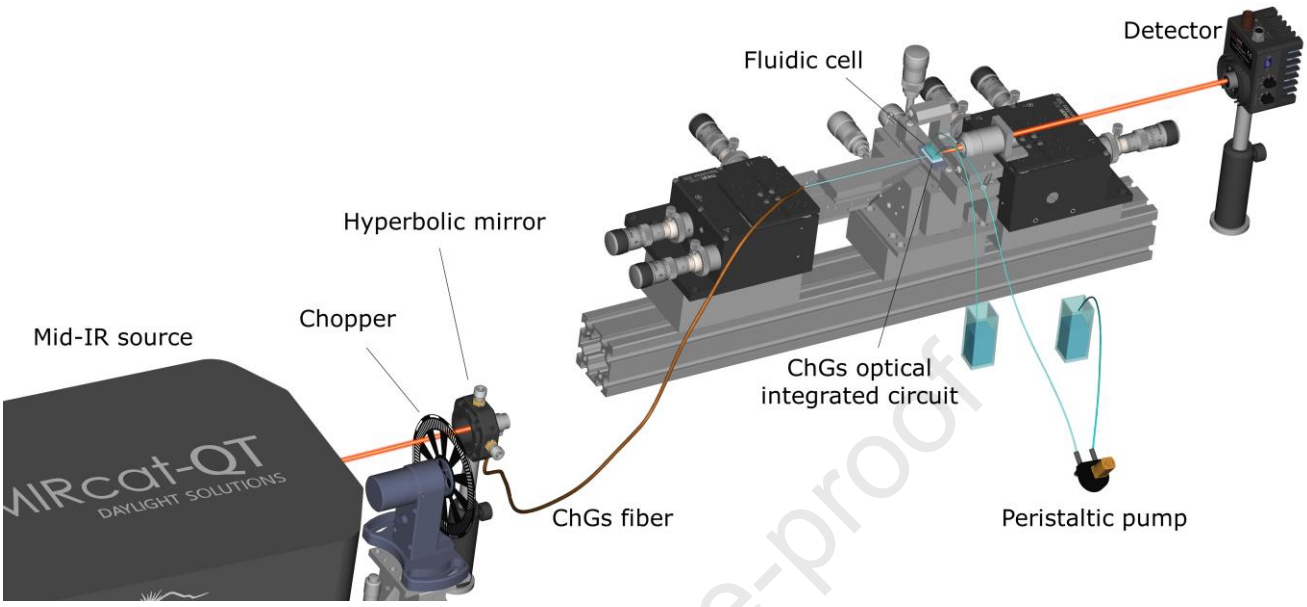

Fig. 2. Schematic of the optical bench setup for optical characterizations.

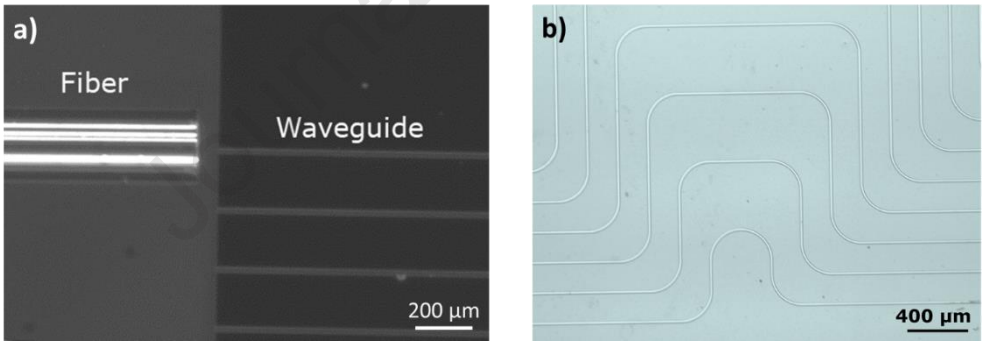

Fig. 3. Microscope image illustrating (a) fiber-waveguide coupling; (b) waveguide length variation for propagation losses measurement by a non-destructive cutback method.

The transmission of the ChGs waveguides was measured in two wavelength ranges using the optical characterization bench displayed in Fig. 2. For the first range (3.9 to 4.6 µm), sample A was used with waveguide lengths ranging from 10 to 15 mm in increments of 0.5 mm. For the second range (7 to 8.95 µm), sample B was used with waveguide lengths ranging from 10.6 to 15.6 mm, also incremented by 0.5

mm. To extract propagation losses, transmission signals measured at each wavelength were adjusted using a decreasing exponential function according to Beer-Lambert's law.

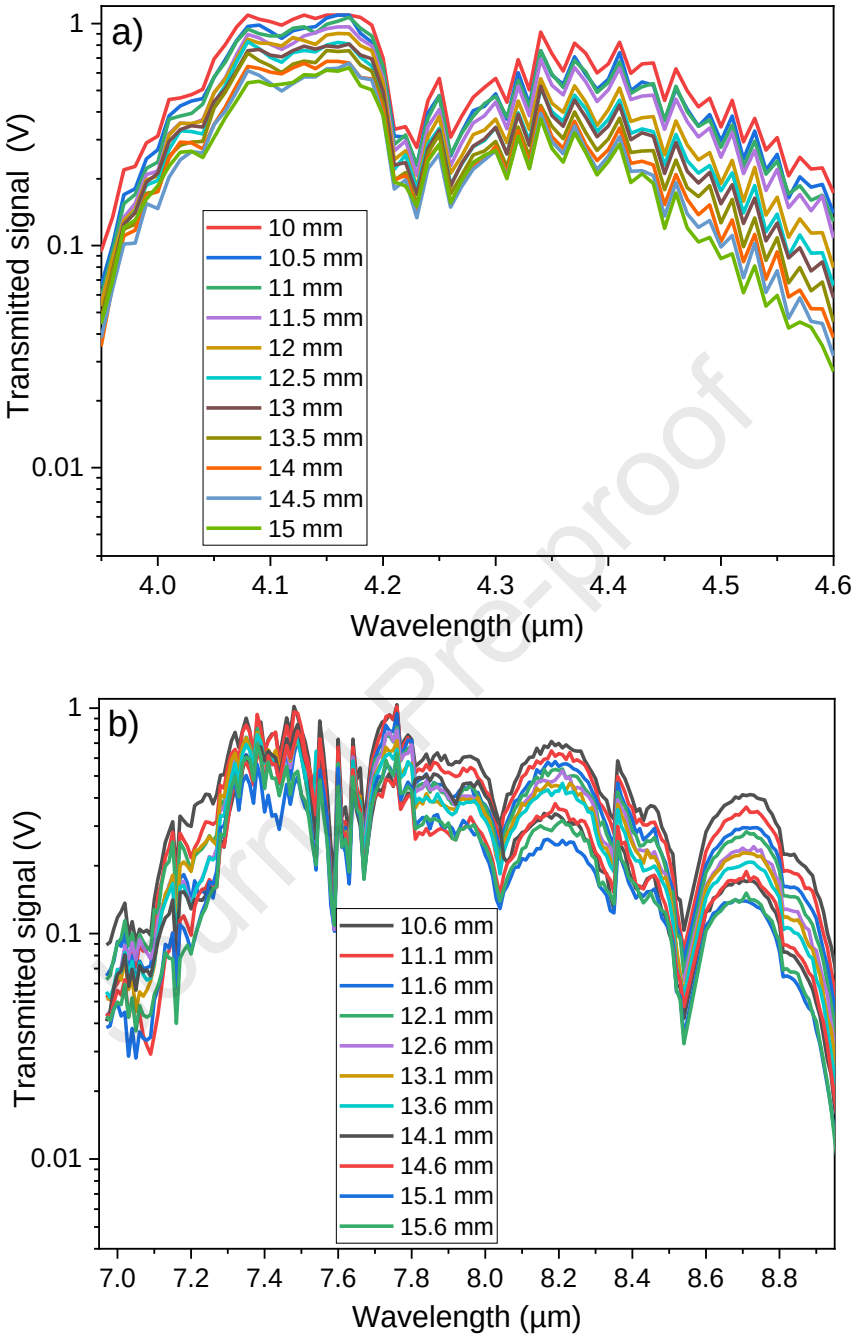

Fig. 4. Transmitted signal amplitude evolution as a function of the wavelength λ for various waveguide lengths obtained with (a) sample A for λ = 3.9 to 4.6 μm (b) sample B for λ = 7.0 to 8.95 μm.

Fig. 4a and 4b show wide transparency range available from 3.9 up to 8.95 µm. The behavior of the transmitted signal can be described by the Beer-Lambert law:

$$P(\lambda) = P_0(\lambda)\, e^{-(\,\varepsilon(\lambda)\,\Gamma(\lambda)\,C\,L_{analyte})}\, e^{-(\,\alpha(\lambda)\,L_{waveguide})} \qquad \text{(eq. 1)}$$

where P_0 is the initial amplitude, ϵ is the molar absorption coefficient, Γ is the external confinement factor, C is the concentration of the analyte, α are the propagation losses, and $L_{waveguide}$ is the length of the waveguide. Since no specific analyte is targeted during propagation losses measurements, the term related to absorption is negligible compared to that of propagation losses ($\epsilon\Gamma C << \alpha$). Moreover, the concentrations of molecules present in the ambient air do not vary significantly during the measurements. Therefore, the first exponential term in eq. 1 can be considered as a constant and included in P_0.

From the adjustment procedure of the measurement points in Fig. 4 with eq. 1, propagation losses are extracted in units of cm^{-1}.

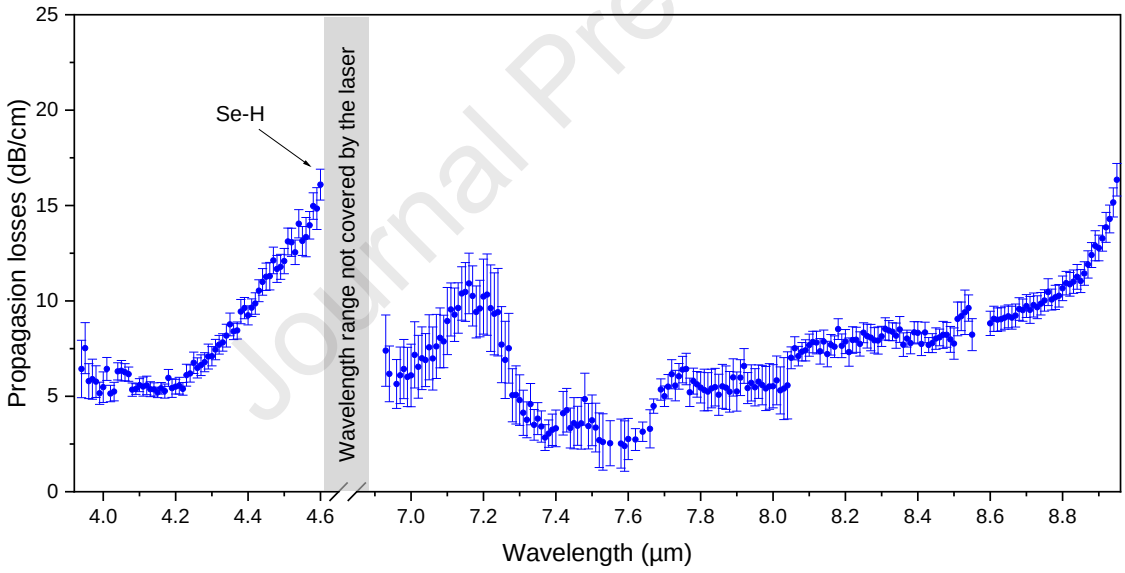

Fig. 5. Propagation losses as a function of the wavelength for ChGs ridge waveguides.

Fig. 5 shows propagation losses that fluctuate between 5 and 7 dB/cm at 3.94 up to 4.03 µm, with relatively large error bars. This variation is attributed to the low power of the laser source in this wavelength range. Between 4.08 and 4.22 µm, the losses stabilize with values between 5.2 and 5.4 dB/cm. However, an increase of propagation losses is observed at longer wavelength, increasing from 6 dB/cm at 4.23 µm to 16 dB/cm at 4.6 µm. Work on chalcogenide glass optical fibers containing selenium has

reported the observation of an absorption peak corresponding to the Se-H bond around λ = 4.6 µm. These hydrogen-related impurities, present at the ppm level, persist in the glass even after purification by several distillations [22,23].

Around λ = 7 µm, the losses are approximately 6 dB/cm, but then, increase with wavelength to reach a local maximum of around 10 dB/cm at λ = 7.2 µm. The losses decrease to reach values of around 2 to 3 dB/cm, with a minimum of 2.52 dB/cm at λ = 7.58 µm. They then increase and stabilize on a stable region between λ = 7.71 and 8.04 µm, with losses values around 5.5 dB/cm. A second stable behavior is observed between λ = 8.05 and 8.55 µm, with losses varying between 7 and 8 dB/cm. The lack of extracted propagation losses observed in the curve between 8.55 and 8.6 µm is due to the low power of the laser source. Finally, the losses increase progressively for wavelengths longer than λ = 8.51 µm, increasing from 9 to 16.4 dB/cm at λ = 8.95 µm.

2.3 Sensing demonstration

The sensing capacity of the ChGs platform was evaluated by conducting transduction tests for both a gas, carbon dioxide (CO_2), and a liquid, isopropanol (IPA). For CO_2 sensing, different concentrations were prepared by diluting CO_2 with nitrogen (N_2) using flexible pipes that provide the mixture from two gas cylinders containing, respectively, 100% concentration of N_2 and CO_2. The flow rates of N_2 and CO_2 gases were regulated using mass flow controllers. To control the light-matter interaction within the ridge waveguide, a PDMS cell with a microchannel (500 µm thick, 5 mm wide, and 28 mm long) was bonded onto the sample after O_2 plasma treatment, as shown in Fig. 6.

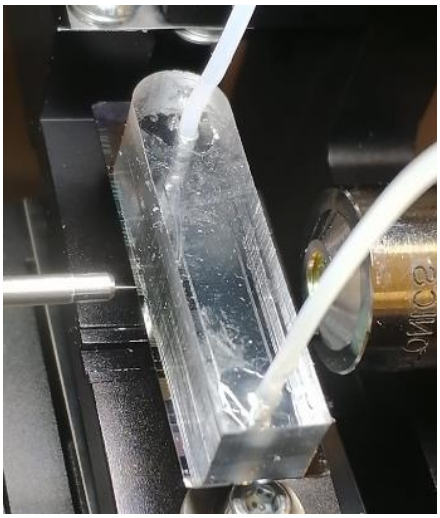

Fig. 6. Fluidic cells mounted on a chalcogenide glass using O_2 plasma treatment.

To highlight CO_2 detection through spectral analysis, the transmission spectra of the ChGs sensor were measured for different concentrations, starting from 0% CO_2 as a reference. Using sample A, the interaction length between the guided light and the gas is 10.8 mm. The maximum recorded absorption peak corresponds to the two absorption lines tabulated at 4.23 and 4.28 µm from the HITRAN database (see Fig. 7a). The normalized transmission spectrum of the ChGs sensor for 35% CO_2 mass concentration is presented in Fig. 7b, covering the wavelength range from 4.14 to 4.33 µm. The measured absorption peaks represent the overlap of the laser's linewidth with the molecule's intrinsic absorption peaks. Since only a small proportion of the dynamic range of the detector is utilized, it would also be interesting to probe with a fixed emission wavelength using one of the two peaks at 4.23 and 4.28 µm to increase measurement sensitivity.

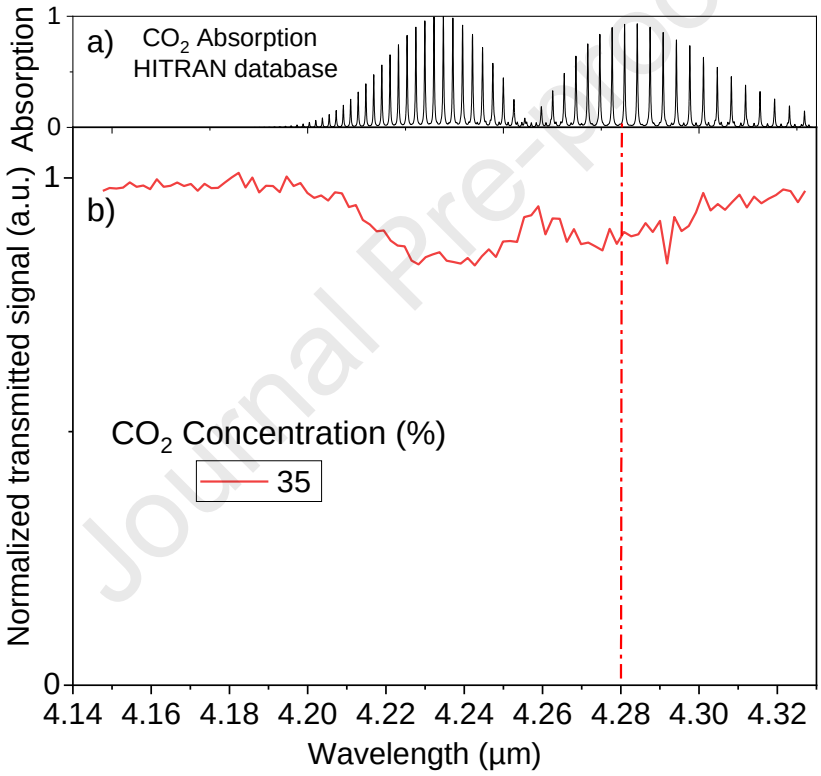

Fig. 7. (a) Normalized CO_2 Absorption from 4.14 to 4.33 µm from HITRAN database [24]. (b) Normalized ChGs waveguide transmission spectra for CO_2 mass concentration fixed at 35%.

The chosen absorption peak for fixed-wavelength CO_2 transduction is λ = 4.28 µm. The signal transmitted by the sensor is recorded for each concentration for at least one min. To ensure the accuracy of the measurements and correctly assign each detector response to the gas mixture present in the cell, pure nitrogen is introduced to evacuate the cell of the previous mixture and return to the initial zero level. This overcomes CO_2 concentration variations caused by external factors, such as the presence of the experimenter during the measurement. Average amplitude and the standard deviation over 60 s of recording for each mass concentration were extracted as shown in Fig. 8.

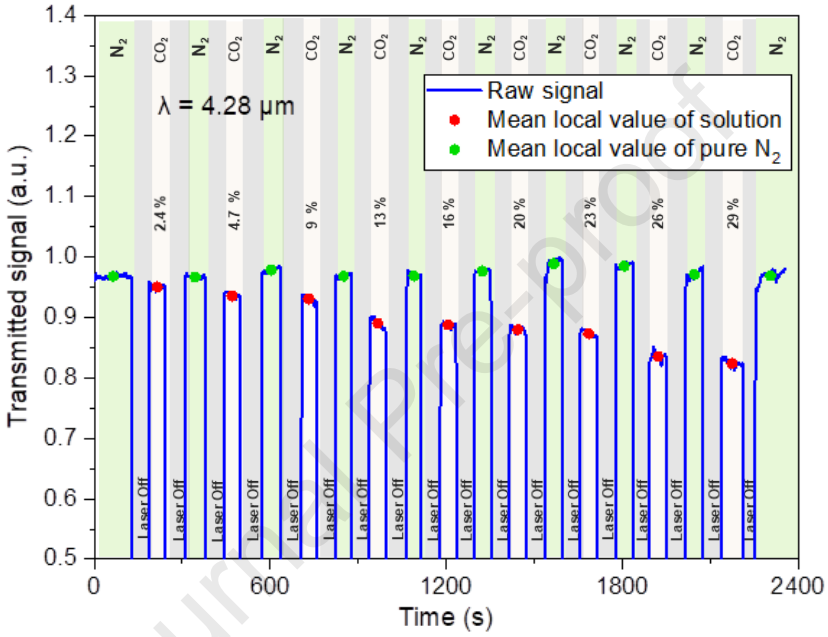

Fig. 8. Evolution of the transmitted signal amplitude at a fixed laser emission (λ = 4.28 µm) with increasing CO_2 mass concentration. The laser beam is interrupted after each concentration change and pure nitrogen is introduced into the fluidic cell.

The data obtained from the measurement are then plotted as a function of the respective concentrations in Fig. 9. This figure shows good agreement with the decreasing exponential fit of the Beer-Lambert law, given by the eq. 2:

$$P(\lambda) = P_0(\lambda)\, e^{-(\varepsilon(\lambda)\, \Gamma(\lambda)\, C\, L)} \qquad \text{(eq. 2)}$$

where P_0 is the initial amplitude, ε is the molar absorption coefficient of CO_2 at λ = 4.28 µm, Γ is the external confinement factor, C is the concentration of CO_2, and L is the interaction length.

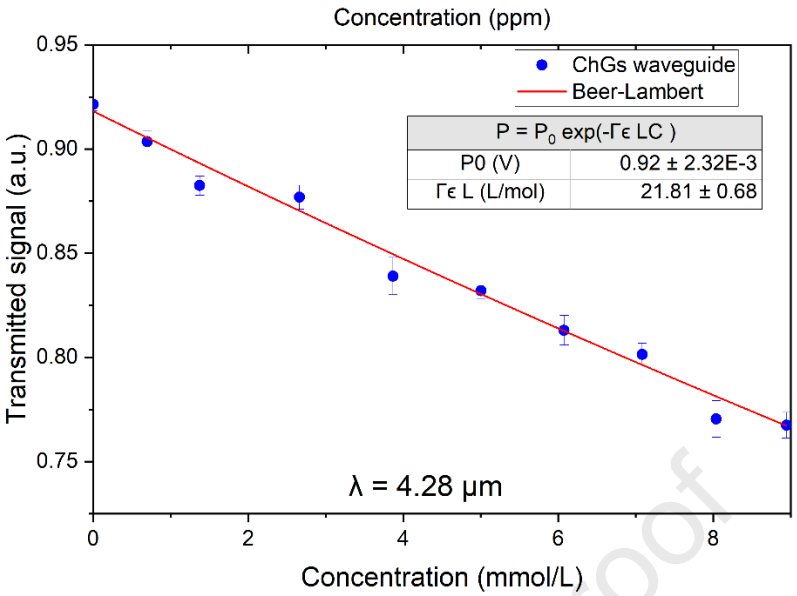

Fig. 9. Transmitted signal through the waveguide as a function of concentration at λ = 4.28 µm.

In order to calculate the LoD, the sensitivity *S* has to be evaluated at the origin of the curve in Fig. 9 (C = 0 mol/L). It can be calculated by differentiating the transmitted signal with respect to concentration:

$$S = \left|\frac{dP}{dC}\right| = \varepsilon \Gamma L P_{(C=0)} \qquad \text{(eq. 3)}$$

The term $\epsilon\Gamma L$ corresponds to the coefficient of the exponential and $P_{C=0}$ is the signal amplitude corresponding to C = 0 mol/L. Using these values, we obtain a sensitivity at the origin of S = 13.4 V.L.mol^{-1}. σ which corresponds to the standard deviation of the signal during the acquisition of the signal amplitude at C = 0 mol/L. We have recorded σ = 3 mV. The LoD is obtained by the following formula [25]:

$$LoD = 3.3\frac{\sigma}{S} \qquad \text{(eq. 4)}$$

The obtained LoD is equal to 4.93×10^{-4} mol/L, which corresponds to a concentration of 1.16%v. Taking into account the responsivity (Volt/Watt) of the detector (*DSS-PSE020TC, Horiba*), which is 2×10^{6} (V/W), the sensitivity is found to be equal to S = 10.05 µW L mol^{-1}.

Parameters of the eq. 2, in particular the product $\varepsilon\Gamma L$, are experimentally extracted, using the adjustment of data presented in Fig. 9 with Beer-Lambert's law. The interaction length L is known and equal to 10.8 mm however the product $\varepsilon\Gamma$ cannot be separated. In the literature, it is mentioned that the molar absorption coefficient ε may not correspond to that of databases, as the laser resolution and the free-space propagation part must be taken into account [26]. For this reason, an additional free-space

experiment, without waveguide, is necessary to estimate the experimental molar absorption coefficient ε using the same experimental conditions (laser linewidth in particular). Through this experiment, the molar absorption coefficient ε is estimated to be (310.7 ± 9.5) L (mol cm)$^{-1}$ at λ = 4.28 µm. In the literature, a measurement made with a laser similar to the one used in this work reported an experimental absorption coefficient ε of 360.1 L (mol cm)$^{-1}$ at λ = 4.23 µm [27]. This value is comparable to the one derived from Fig. 9.

Since the absorption coefficient ε is estimated, it is now possible to experimentally extract the external confinement factor Γ, which turns out to be equal to (6.5 ± 0.2)%. This value falls within the range of the simulation values of Γ obtained from commercial software (*FIMMWAVE, Photon Design*), which are between Γ_{TE} = 9.1% and Γ_{TM} = 1.4%. It has already been noted that controlling the polarization of the guided mode is challenging due to the use of an optical fiber for coupling into the waveguide. However, we maintain the same polarization throughout all measurements to ensure sensing accuracy.

In the case of liquid phase transduction tests, a peristaltic pump was used to control the flow of liquids through the fluidic cell as shown in Fig. 2 bonded to sample B. Its ability to provide very low flow rates makes it an ideal choice for preserving the integrity of the fluidic circuit of the integrated sensor during transduction measurements.

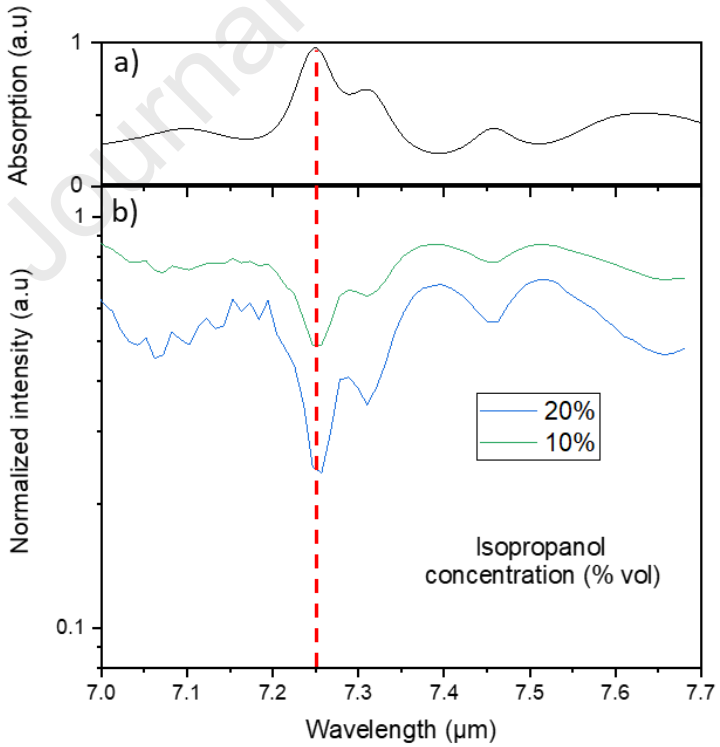

Fig. 10. (a) Normalized absorption spectrum of IPA from λ = 7 to 7.7 µm [28]; (b) Normalized transmission spectrum of IPA diluted in cyclohexane with different concentrations.

For IPA sensing, different concentrations are prepared by diluting it in cyclohexane, transparent solvent in the operating wavelength range. According to database [28], IPA displays an absorption peak centered at λ = 7.25 µm (Fig. 10a). This absorption peak is also observed in the transmission spectra measured with the ChGs platform (Fig. 10b), with a curve shape that closely matches the absorption curve in the database. The interaction length here is equal to 5.8 mm.

The absorption peak located at λ = 7.25 µm is chosen for the fixed wavelength transmission measurement. The transmitted signal through the waveguide, which is recorded for each concentration for 20 s. To ensure the accuracy of the measurements and correctly assign each detector response to the solution present in the cell, an air flow is introduced into the fluidic circuit after each concentration change. It is important to consider that a small amount of the previous solution may remain in the fluidic channel during a measurement. Numerical processing was performed to extract points from the raw signal corresponding to each concentration by averaging over 15 last seconds before each change in concentration. These points are plotted on Fig. 11.

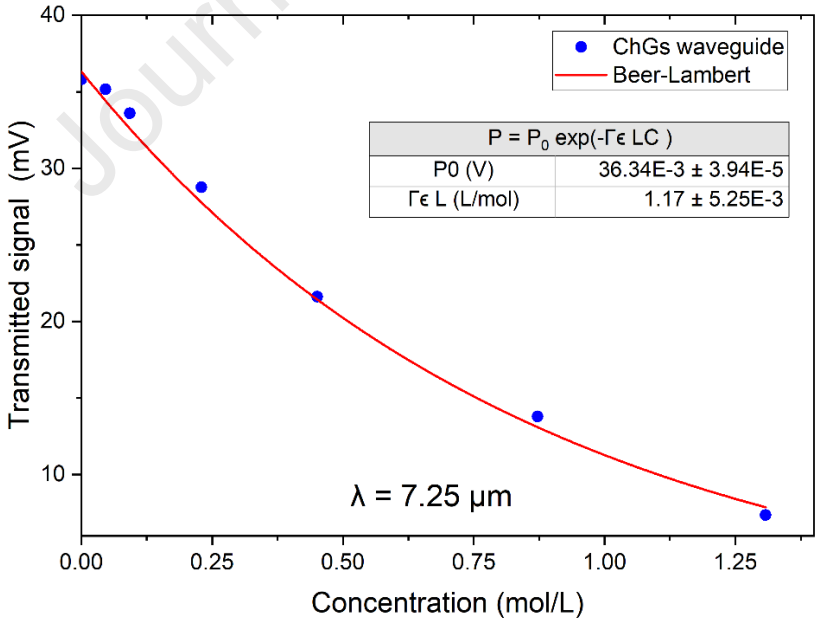

Fig. 11. Signal amplitude as a function of IPA concentration diluted in cyclohexane for a fixed wavelength at λ = 7.25 µm with an interaction length L = 5.8 mm.

By applying an exponential Beer-Lambert fit, parameters related to the transduction of IPA in cyclohexane were obtained. With a standard deviation of the signal at C = 0 mol L^{-1} of 48.3 µV, the sensitivity of our measurement system was estimated to 1.55 nW L mol^{-1} and, a LoD of 300 ppmv (3.8 mmol L^{-1}) was obtained.

3. Discussion

The waveguides used in this study exhibit higher propagation losses compared to other platforms, such as Ge [29] and SiGe [30]. However, these platforms are not as transparent as ChGs in the mid-IR. While arsenic based ChGs compositions demonstrate lower propagation losses, below 1 dB/cm [31], the use of arsenic poses significant environmental concerns.

Impurities can significantly contribute to absorption, thereby increasing optical losses. Specifically, the absorption bands associated with Se-H, Ge-O, and Sb-O are notable. These impurities are typically present in concentrations ranging from approximately 20 to 1000 ppm. The losses values are also closely related to the roughness state of the sidewalls of the guiding structures. Since the propagation here is single mode, a part of the optical mode interacts strongly with the surfaces defined by the waveguide. A high roughness at the level of these surfaces can lead to significant propagation losses. In addition to the roughness of the sidewalls of the guiding structures, the variation in propagation losses may be attributed to the presence of chemical substances on the waveguides [20], particularly residues of fluoropolymers, which absorb light around the working wavelength range [32]. It is believed that these fluoropolymers can be deposited on the waveguide sidewalls during the dry etching process based on fluorine chemistry. The absorption of these fluoropolymers has already been demonstrated in the literature by Ma et al. [13], who used a $Ge_{11.5}As_{24}Se_{64.5}$ waveguide.

The propagation loss values measured in this work are comparable to those of other ChGs platforms used for sensing applications. Table 2 compares the transduction measurement characteristics of CO_2 performed with the ChGs platform with other works.

Table 2. Characteristics of the gas sensor using the ChGs platform compared with the literatures.

Gas	λ (µm)	ChGs Composition	Interaction length (cm)	losses (dB/cm)	Γ (%)	LoD (ppmv)	Ref.
CH_4	3.31	$Ge_{23}Sb_7S_{70}$	2	7	8	25000	[33]
CH_4	3.31	$Ge_{23}Sb_7S_{70}$	0.5	8	12.5	10000	[20]
CO_2	4.319	$Ge_{28}Sb_{12}Se_{60}$	1	5.1	4.6	25000	[34]

Journal Pre-proof

CO_2	4.28	$Ge_{12.6}Sb_{25.2}Se_{62.2}$	1.08	6.8	6.5	11600	This work

These studies were all conducted by direct absorption spectroscopy (DAS) using ChGs waveguides in a ridge or rib configurations. Propagation losses values reported by different research teams are comprised between 5.1 and 8 dB/cm. Regarding external confinement factors, their range of variation extends from 4.6% to 12.5%. It should be noted that these values are often obtained from numerical simulations, which makes the comparison less robust compared to propagation losses measured in this work, which are experimental measurements.

The LoD of 11600 ppmv that we obtained with the ChGs platform is comparable to that reported in *Tab. 2*, which is between 10000 and 25000 ppmv. However, this value is large compared to alternative platforms. LoD of 500 ppmv was reported with a Si waveguide [26], another LoD of 1000 ppmv with a partially suspended Si waveguide [35], and a value of 3.25 ppmv is reached with a Ge slot waveguide [36]. These results suggest that improvements can still be achieved with ChGs structures to improve transduction and further reduce the detection limit. Furthermore, propagation losses can be reduced by improving the surface state of the guiding structures with optimized gas mixture during etching processes. Some techniques can be employed to enhance sensing performance. For instance, in Reference [34] in Table 2, the LoD achieved using the wavelength modulation spectroscopy (WMS) technique was 3000 ppmv for CO_2, which is 8 times lower than that obtained using DAS.

A ChGs waveguide with silver island film was used to produce surface-enhanced infrared absorption (SEIRA) effect for CH_4 sensing at 3.29 µm [14]. In this case, the LoD was achieved 6100 ppmv.

Table 3. Comparison of transduction performances of the ChGs platform with literature for the detection of molecules in liquid phase.

Molecules	λ (µm)	Structure	Interaction length (cm)	Losses (dB/cm)	Γ (%)	LoD (ppmv)	Ref.
IPA	3.73	ChGs	0.402	7.86	12.8	50000	[37]
IPA	7.215	Diamant	0.5	5	-	650	[38]
IPA	7.25	ChGs	0.58	7.7	6.5	300	This work

Table 3 compares the isopropanol transduction characteristics of the ChG platform with those reported in the literature. It has been reported the detection of isopropanol in acetone at a volume concentration of 5% with a germanium waveguide deposited on SiN at λ = 3.73 µm, with propagation losses of 7.86 dB/cm [37]. However, the high concentration in this reference can be explained by the low absorption of isopropanol at λ = 3.73 µm, compared to λ = 7.25 µm. Another study reported a diamond waveguide with losses of 5 dB/cm at λ = 7.215 µm, used for the detection of isopropanol with a LoD of 650 ppmv [38], which is higher than the LoD obtained in this paper.

4. Conclusion

In conclusion, this work demonstrated the performance of mid-infrared ChGs PICs for evanescent wave transduction. The ridge fabricated ChGs waveguides exhibited a wide transparency range from λ = 3.94 to 8.95 µm, with minimum propagation losses of 2.5 dB/cm at λ = 7.58 µm. In addition to the sidewall roughness of the waveguides, the variation in propagation losses values over the remaining wavelength range is due to the presence of impurities backgrounds in the chalcogenide glasses, but also to the presence of fluoropolymers resulting from the use of fluorinated gases during the etching of the ChGs layers. The etching process of ChGs is currently under study in order to eliminate fluoropolymers and reduce the waveguides propagation losses.

To validate the feasibility of the suggested sensor, a gas sensing experiment was conducted using CO_2, resulting in an estimated LoD of 11600 ppmv at λ = 4.28 µm. Furthermore, the liquid sensing experiment conducted at λ = 7.25 µm using isopropanol as the analyte in a cyclohexane solvent, demonstrated a LoD of 300 ppmv. To further lower the LoD, the implementation of WMS is also being considered. This will require replacing the laser source with another source featuring a linewidth narrower than the CO_2 absorption band.

Furthermore, integrated optics allow for the development of advanced on-chip photonic structures, such as ring resonators and Mach-Zehnder interferometers, which provide inherent molecular detection, and the high analytical sensitivity required for next-generation sensors.

The versatility of the ChG platform, with wavelength dependent tunability achieved by adjusting the dimensions of its guiding structures, offers numerous opportunities for sensing applications. Its capacity to operate across a critical wavelength range, aligning with the atmospheric windows of 4–5 µm and 8–12 µm, enables efficient sensing in both gas and liquid environments. Additionally, the platform's strong agreement with theoretical predictions for the external confinement factor further validates its accuracy and its reliability.

Funding

This work was supported by the French national research agency under AQUAE ANR project (ANR ANR-21-CE04-011) and project IBAIA, funding from the European Union's Horizon Europe Framework Programme under grant agreement No. 101092723. Equipment funding of Institut Foton was partly provided by the CPER Sophie, Région Bretagne and Lannion Tregor Communauté.

Acknowledgments

ChGs layers were deposited at Institute des Sciences Chimiques de Rennes (ISCR) whereas ridge waveguides processing was performed in the Centre Commun Lannionnais d'Optique (CCLO) clean room facilities of Foton Institute. This work was partly supported by the French Renatech + network.

Disclosures

The authors declare no conflicts of interest.

References

[1] Baudet E, Gutierrez-Arroyo A, Němec P, Bodiou L, Lemaitre J, De Sagazan O, et al. Selenide sputtered films development for MIR environmental sensor. Opt Mater Express 2016;6:2616. https://doi.org/10.1364/ome.6.002616.

[2] Lucas J, Troles J, Zhang XH, Boussard-Pledel C, Poulain M, Bureau B. Glasses to see beyond visible. Comptes Rendus Chimie 2018;21:916–22. https://doi.org/10.1016/j.crci.2018.02.010.

[3] Bureau B, Boussard C, Cui S, Chahal R, Anne ML, Nazabal V, et al. Chalcogenide optical fibers for mid-infrared sensing. Opt Eng 2014;53:027101. https://doi.org/10.1117/1.OE.53.2.027101.

[4] Snopatin GE, Shiryaev VS, Plotnichenko VG, Dianov EM, Churbanov MF. High-purity chalcogenide glasses for fiber optics. Inorg Mater 2009;45:1439. https://doi.org/10.1134/S0020168509130019.

[5] Sanghera J, Gibson D. Optical properties of chalcogenide glasses and fibers. Chalcogenide Glasses, Elsevier; 2014, p. 113–38. https://doi.org/10.1533/9780857093561.1.113.

[6] Ali S, Karine Le F, Alain V. Photoinduced bragg reflectors in As-S-Se/As-S based chalcogenide glass multilayer channel waveguides. Fiber and Integrated Optics 2001;20:151–8. https://doi.org/10.1080/01468030117935.

[7] Tasseva J, Lozanova V, Todorov R. Linear and non-linear optical properties of GeS_2 doped with the elements from III and V group of the periodic table. Bulg Chem Commun 2013;45:33–7.

[8] Zhou G, Chen J, Su C, Gao C, Kang S, Tan L, et al. Multilayered chalcogenide glass with gradient index for reduced SWaP IR optical system. Ceram Int 2023;49:32843–9. https://doi.org/10.1016/j.ceramint.2023.07.255.

[9] Bodiou L, Starecki F, Lemaitre J, Nazabal V, Doualan JL, Baudet E, et al. Mid-infrared guided photoluminescence from integrated Pr^{3+}-doped selenide ridge waveguides. Optical Materials 2018;75:109–15. https://doi.org/10.1016/j.optmat.2017.10.001.

[10] Bodiou L, Baillieul M, Nazabal V, Lemaitre J, Benardais A, Meziani S, et al. Carbon dioxide mid-infrared sensing based on Dy^{3+}-doped chalcogenide waveguide photoluminescence. Opt Lett 2023;48:1128–31. https://doi.org/10.1364/OL.483613.

[11] Pelusi MD, Ta'eed VG, Libin Fu, Magi E, Lamont MRE, Madden S, et al. Applications of highly-nonlinear chalcogenide glass devices tailored for high-speed all-optical signal processing. IEEE J Select Topics Quantum Electron 2008;14:529–39. https://doi.org/10.1109/JSTQE.2008.918669.

[12] Ta'eed VG, Baker NJ, Fu L, Finsterbusch K, Lamont MRE, Moss DJ, et al. Ultrafast all-optical chalcogenide glass photonic circuits. Opt Express 2007;15:9205–21. https://doi.org/10.1364/OE.15.009205.

[13] Ma P, Choi DY, Yu Y, Gai X, Yang Z, Debbarma S, et al. Low-loss chalcogenide waveguides for biosensing in the mid-infrared. Opt Express 2013;21:29927-37. https://doi.org/10.1364/OE.21.029927

[14] Pi M, Zheng C, Ji J, Zhao H, Peng Z, Lang J, et al. Mid-infrared Chalcogenide Waveguide CH_4 Sensor Based on Surface-enhanced Infrared Absorption Spectroscopy. 2022 Photonics & Electromagnetics Research Symposium (PIERS), 2022, p. 214–8. https://doi.org/10.1109/PIERS55526.2022.9793156.

[15] Mittal V, Sessions NP, Wilkinson JS, Murugan GS. Optical quality ZnSe films and low loss waveguides on Si substrates for mid-infrared applications. Opt Mater Express 2017;7:712–25. https://doi.org/10.1364/OME.7.000712.

[16] Ma P, Choi DY, Yu Y, Yang Z, Vu K, Nguyen T, et al. High Q factor chalcogenide ring resonators for cavity-enhanced MIR spectroscopic sensing. Opt Express 2015;23:19969. https://doi.org/10.1364/OE.23.019969.

[17] Sieger M, Mizaikoff B. Toward On-Chip Mid-Infrared Sensors. Anal Chem 2016;88:5562–73. https://doi.org/10.1021/acs.analchem.5b04143.

[18] Veldhuis GJ, Parriaux O, Hoekstra HJWM, Lambeck PV. Sensitivity enhancement in evanescent optical waveguide sensors. Journal of Lightwave Technology 2000;18:677–82. https://doi.org/10.1109/50.842082.

[19] Mittal V, Nedeljkovic M, Rowe DJ, Murugan GS, Wilkinson JS. Chalcogenide glass waveguides with paper-based fluidics for mid-infrared absorption spectroscopy. Opt Lett 2018;43:2913–6. https://doi.org/10.1364/OL.43.002913.

[20] Su P, Han Z, Kita D, Becla P, Lin H, Deckoff-Jones S, et al. Monolithic on-chip mid-IR methane gas sensor with waveguide-integrated detector. Appl Phys Lett 2019;114:051103. https://doi.org/10.1063/1.5053599.

[21] Qiao L, Zheng Z, Sun W. A Study on SF6 Gas Sensor on MEMS. 2020 IEEE International Conference on Artificial Intelligence and Computer Applications (ICAICA), 2020, p. 1087–90. https://doi.org/10.1109/ICAICA50127.2020.9182628.

[22] Wang X, Jiao K, Farrell G, Wang X. Chalcogenide Glass Preparation, Purification and Fiber Fabrication. In: Wang P, Wang X, Guo H, Zhang P, Wang S, Jia S, et al., editors. Mid-Infrared Fluoride and Chalcogenide Glasses and Fibers, Singapore: Springer Nature; 2022, p. 99–171. https://doi.org/10.1007/978-981-16-7941-4_5.

[23] Bureau B, Maurugeon S, Charpentier F, Adam JL, Boussard-Plédel C, Zhang XH. Chalcogenide glass fibers for infrared sensing and space optics. Fiber Integr Opt 2009;28:65–80. https://doi.org/10.1080/01468030802272542.

[24] Gordon IE, Rothman LS, Hill C, Kochanov RV, Tan Y, Bernath PF, et al. The HITRAN2016 molecular spectroscopic database. J Quant Spectrosc Radiat Transfer 2017;203:3–69. https://doi.org/10.1016/j.jqsrt.2017.06.038.

[25] Pack BW, Stithit S, Chen W. Clinical supplies manufacture. Developing Solid Oral Dosage Forms, Elsevier; 2017, p. 653–76. https://doi.org/10.1016/B978-0-12-802447-8.00024-8.

[26] Ranacher C, Consani C, Vollert N, Tortschanoff A, Bergmeister M, Grille T, et al. Characterization of evanescent field gas sensor structures based on silicon photonics. IEEE Photonics J 2018;10:1–14. https://doi.org/10.1109/JPHOT.2018.2866628.

[27] Ranacher C, Consani C, Tortschanoff A, Jannesari R, Bergmeister M, Grille T, et al. Mid-infrared absorption gas sensing using a silicon strip waveguide. Sens. Actuators, A 2018;277:117–23. https://doi.org/10.1016/j.sna.2018.05.013.

[28] Myers TL, Tonkyn RG, Danby TO, Taubman MS, Bernacki BE, Birnbaum JC, et al. Accurate measurement of the optical constants n and k for a series of 57 inorganic and organic liquids for

optical modeling and detection. Appl Spectrosc 2018;72:535–50. https://doi.org/10.1177/0003702817742848.

[29] Mashanovich GZ, Mitchell CJ, Penades JS, Khokhar AZ, Littlejohns CG, Cao W, et al. Germanium mid-Infrared photonic devices. J Lightwave Technol 2017;35:624–30. https://doi.org/10.1109/JLT.2016.2632301.

[30] Montesinos-Ballester M, Vakarin V, Liu Q, Roux XL, Frigerio J, Ballabio A, et al. Ge-rich graded SiGe waveguides and interferometers from 5 to 11 μm wavelength range. Opt Express 2020;28:12771–9. https://doi.org/10.1364/OE.391464.

[31] Hô N, Phillips MC, Qiao H, Allen PJ, Krishnaswami K, Riley BJ, et al. Single-mode low-loss chalcogenide glass waveguides for the mid-infrared. Opt Lett 2006;31:1860–2. https://doi.org/10.1364/OL.31.001860.

[32] Saito M, Gojo T, Kato Y, Miyagi M. Optical constants of polymer coatings in the infrared. Infrared Phys Technol 1995;36:1125–9. https://doi.org/10.1016/1350-4495(95)00042-9.

[33] Han Z, Lin P, Singh V, Kimerling L, Hu J, Richardson K, et al. On-chip mid-infrared gas detection using chalcogenide glass waveguide. Appl Phys Lett 2016;108:141106. https://doi.org/10.1063/1.4945667.

[34] Pi M, Zheng C, Zhao H, Peng Z, Lang J, Ji J, et al. Mid-infrared ChG-on-MgF_2 waveguide gas sensor based on wavelength modulation spectroscopy. Opt Lett 2021;46:4797–800. https://doi.org/10.1364/OL.440361.

[35] Ottonello-Briano F, Errando-Herranz C, Rödjegård H, Martin H, Sohlström H, Gylfason KB. Carbon dioxide absorption spectroscopy with a mid-infrared silicon photonic waveguide. Opt Lett 2020;45:109–12. https://doi.org/10.1364/OL.45.000109.

[36] Shim J, Lim J, Geum DM, Kim BH, Ahn SY, Kim S. Tailoring bolometric properties of a TiO_x /Ti/TiO_x tri-layer film for integrated optical gas sensors. Opt Express 2021;29:18037. https://doi.org/10.1364/OE.427147.

[37] Li W, Anantha P, Lee KH, Qiu HD, Guo X, Goh SCK, et al. Spiral waveguides on germanium-on-silicon nitride platform for mid-IR sensing applications. IEEE Photonics Journal 2018;10:1–7. https://doi.org/10.1109/JPHOT.2018.2829988.

[38] Forsberg P, Hollman P, Karlsson M. High sensitivity infrared spectroscopy with a diamond waveguide on aluminium nitride. Analyst 2021;146:6981–9. https://doi.org/10.1039/D1AN01009C.

Journal Pre-proof

Declaration of interests

☒ The authors declare that they have no known competing financial interests or personal relationships that could have appeared to influence the work reported in this paper.

☐ The authors declare the following financial interests/personal relationships which may be considered as potential competing interests:

Journal Pre-proof